Géotechnique **00**, 1–15 [http://dx.doi.org/10.1680/geot.XX.XXXXX]

Effect of grain size distribution on the shear band thickness evolution in sand

H. RATTEZ*, Y. SHI†, A. SAC-MORANE‡, T. KLAEYLE‡, B. MIELNICZUK* AND M. VEVEAKIS*

Triaxial experiments have been conducted on granular materials presenting uniform, graded and fractal particle distributions in order to investigate how the broadness of the distribution affects the phenomenon of strain localization. The shear band thickness evolution is assessed by Digital Image Correlation (DIC) using 3 cameras placed at different angles around a transparent triaxial cell. From the field of deformation, gaussian distributions have enabled to fit the data satisfactorily and determine the shear band width evolution. The latter exhibits a rapid decrease in the softening regime until reaching a residual value in all cases. In the conditions of the experiments, it is shown that the residual shear band thickness scales with the mean grain size and the ratio between the two increases with the broadness of the distribution. Samples with uniform distribution exhibit an average residual thickness of $\sim 10D_{50}$, samples with graded distribution exhibit an average residual thickness of $\sim 12.5D_{50}$ and samples with fractal distribution exhibit an average residual thickness of $\sim 17D_{50}$.

KEYWORDS: Sands; Laboratory tests; Failure; Deformation

INTRODUCTION

Strain localization is a pervasive phenomenon observed in many materials characterized by a loss of homogeneity of the field of deformation (Hill, 1962; Rudnicki and Rice, 1975; Vardoulakis and Sulem, 1995). In the particular case of geomaterials, this feature often occurs in the form of shear bands observed experimentally (Desrues and Viggiani, 2004) or on site (Sibson, 2003) accompanying the deformation of retaining walls (Borja and Lai, 2002), footings (Siddiquee et al., 1999), cavities (Pardoen and Collin, 2017), landslides (Segui et al., 2019) or fault zones (Rattez et al., 2018c; Rattez and Veveakis, 2020). The characterization of the size of the zone where most of the deformation concentrates is therefore a key parameter to predict the mechanical behaviour of geomaterials and model many applications involving geomaterials. Indeed, strain localization is usually correlated with a strength weakening of the material.

Many experimental studies have focused on the observation of strain localization using photogrammetry (Desrues and Viggiani, 2004), strain markers (Rathbun and Marone, 2010; Smith et al., 2015), X-ray microtomography coupled with digital volume correlation (Hall et al., 2010; Takano et al., 2015; Desrues et al., 2018) or void ratio maps (Desrues et al., 1996), microscopy on specimen's slices (Smith et al., 2015), and digital image correlation applied to pictures by digital cameras of the external surface of the specimen (Rechenmacher and Finno, 2004; Bhandari et al., 2012). These methods can be sorted into two groups: (i) the observation of a variation of a property like the porosity or a marker at the end of the experiment, (ii) the assessement of the rate of deformation by estimating how a local pattern identified on a picture or scan of the sample has moved compared to one taken at a later stage. The latter methods allow obtaining an evolution and a better estimation of the process of localization. Most of the experimental results for strain localization in sands were obtained for granular materials presenting a narrow grain size distribution (Roscoe, 1970; Scarpelli and Wood, 1982; Mühlhaus and Vardoulakis, 1987; Tatsuoka et al., 1990; Viggiani et al., 2001; Desrues et al., 2018). However, the phenomenon of grain breakage can affect the grain size distribution when intergranular forces exceed the individual particle strength. This phenomenon can be observed for relatively low stress for carbonate materials (Coop et al., 2004). Several studies have focused on the evolution of particle size distribution and it is commonly accepted that the distribution tends toward a residual distribution that is called fractal, which exhibits a wide distribution of grain diameters (Sammis et al., 1987; Einav, 2007; Rattez et al., 2019). Therefore, wide distributions of particles are a common occurence in e.g., fault zones, landslides or at the tip of piles during penetration and in these applications strain localization is also an important phenomenon.

Moreover, the finite thickness of the localized zone cannot be captured with the classical cauchy continuum framework (Vardoulakis, 1985) and the methods that enable to regularize this problem require the introduction of an internal length into the constitutive laws (Sulem et al., 2011; Papanicolopulos and

Manuscript received. . .
*Civil and Environmental Engineering Department, Duke University, Durham, NC, USA.
†Wuhan University, Wuhan, China.
‡Ecole Normale Supérieure Paris-Saclay, Cachan, France.
corresponding author: Hadrien Rattez (Address: Hudson Hall Annex, Room No. 053A Duke University, Durham 27707, NC, USA. email: hadrien.rattez@duke.edu. Phone: +1 (919) 684 5867)

Veveakis, 2011; Rattez et al., 2018a). Most of the existing laboratory experiments and dicrete element simulations that have been used to calibrate these constitutive descriptions have been performed with a relatively narrow grain size distribution. In this case, the internal length of the enriched continuum theory can be identified as the mean grain size D_{50} (Mühlhaus and Vardoulakis, 1987; Ehlers and Scholz, 2007; Veveakis et al., 2012, 2013; Rattez et al., 2018b). The above considerations lead to the following open questions regarding the interplay between shear band thickness and grain size distribution: (i) Is the shear band thickness only controlled by D_{50} or does it depend upon the whole grain size distribution? (ii) What is the role of very fine grains in the localization process? (iii) What appropriate material length should be considered for very wide grain size distribution?

In an attempt to address these questions, triaxial experiments have been conducted in this study on granular materials presenting uniform, graded and fractal particle distributions. The standard triaxial load path and the same initial void ratio, which are important factors for strain localization (Guo and Zhao, 2014, 2016), have been considered for this campaign in order to isolate the effect of the grain size distribution. Digital Image Correlation applied on the pictures taken by 3 cameras placed at different angles around a see-through triaxial cell has enabled to assses the field of deformation on the membrane of the specimens. This simple methodology provides an efficient tool to characterize the shear band evolution during the mechanical tests performed on the specimens presenting different particle size distributions. The experimental setup, the granular samples used and the methodology to estimate the shear band thickness in this study are presented in the first part. Then, the reproducibility of the method is shown, togeteher with the results for the mechanical response and the shear band evolutions obtained.

EXPERIMENTAL SETUP

Standard triaxial experiments (with a Humboldt Masterloader HM-3000 frame) have been conducted on dry sand for the same confining pressure to observe the effect of the change of grain size distribution on the shear band thickness. During the samples preparation, a negative pressure was first applied to the latex membrane. The sand specimens were built by successive layers, which were tamped to achieve a similar weight of sand introduced in the different specimens and, therefore, a similar void ratio and dry unit weight (1600 kg/m^3 here). The specimens present dimensions of 70 mm for the diameter and 140 mm for the height. A constant confining pressure of 275 kPa (40 PSI) is applied to all the specimens with the cell filled with deaereted water. A constant axial strain rate equal to 2 mm/min is applied vertically by the translation of the bottom plate (see Fig. 1.a), which corresponds to an axial deformation (strain) rate of approximately 2.4×10^{-4} s^{-1}. This deformation rate has been chosen to allow enough time between the pictures taken of the sample and for the tests to not last too long. Moreover, at this range of pressure, a silica sand loaded with a constant strain rate does not exhibit a dependency of the mechanical behavior with the strain rate (Tatsuoka et al., 2002). The load is measured by a S-type load cell (Humboldt HM-2300.100). The displacements are retrieved from the displacement of the frame piston (which has been calibrated beforehand with an LVDT). The top cap of the sample is a rotating type, which favors the occurence of one shear band compared to a rigid top cap. No lubrification has been applied to the sample, an effect that has been shown to influence the experimental results (Zhao and Guo, 2015).

Three digital single-lens reflex cameras (Canon 4000D) have been placed 30 cm away from the transparent cell with an angle of 90 degrees between them (see Fig. 1.b), in order to have at least one camera that can capture the shear band when localization is triggered. The software digiCamControl has enabled to synchronize the three cameras and retrieve the pictures digitally every 30 seconds, which corresponds to a total displacement of 1 mm applied to the sample between two successive pictures.

Triaxial DIC setup

The field of incremental displacements is measured using image analysis and in particular DIC. For this methodology, images of the specimen are captured during the mechanical test at various stages of loading (every 30 s here). Then, the pictures from the same point of view are analyzed using a numerical correspondence technique to identify the most similar patterns between successive images (see Figure 2 for an example of a picture and the field of vertical deformation associated). For this method to be efficient, the patterns must remain approximately constant between consecutive images and the local textural information be unique, that is why a random speckle pattern has been applied onto the membrane with a black spray paint. After accounting for possible errors in the image analysis (see Appendix A), Normalized Cross-Correlation has been used, which is a simple and fast method to correlate two images (Haralick and Shapiro, 1992; Lewis, 1995). Other types of cross correlation have been developed (as well as other families of pattern matching) to avoid limitations due to imaging scale, rotation, and perspective distortions, but Normalized Cross-Correlation is in common use in geotechnical applications and performs well even for 3D applications like digital volume correlation of X-ray μCT scans (Andò, 2013).

In these tests, even though pictures are taken from three angles, the image correlation is applied to the set of images from only one camera that has enabled to obtain the clearest view on the shear band. Moreover, the DIC is applied to a window at the center of the pictures (the red rectangle shown in Figure 2. a) to avoid refraction effects that are important on the sides of the sample (Bhandari et al., 2012), as also shown in Appendix A, and to focus on a zone that is included inside the specimen all along the test. This window is chosen indepedently

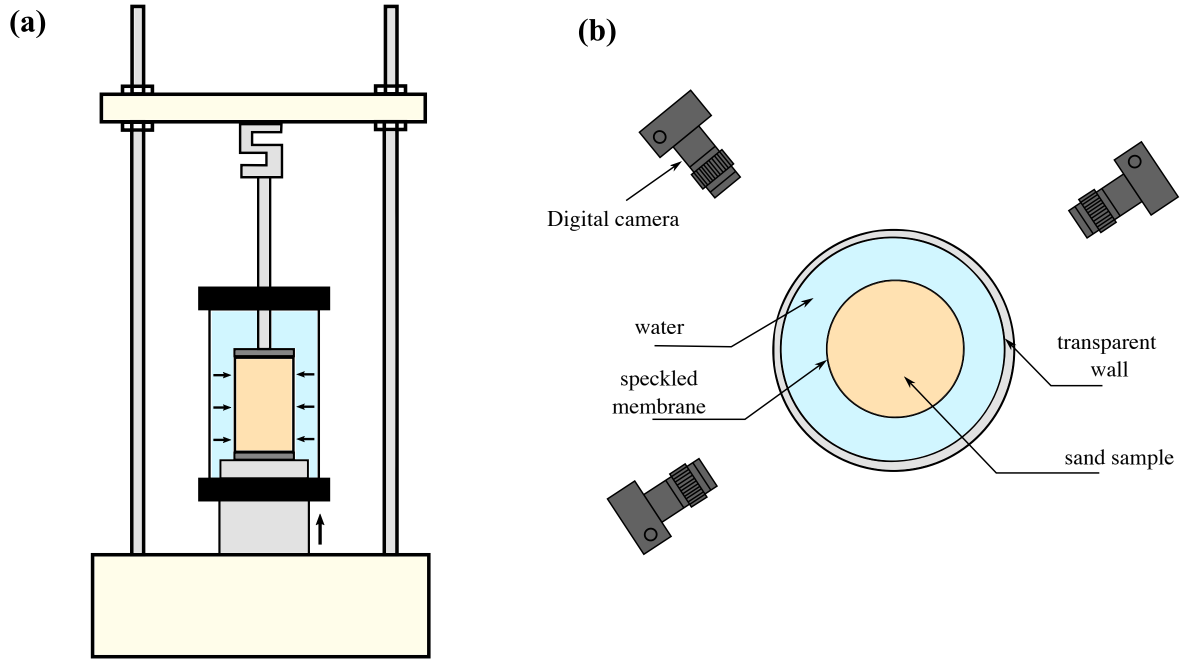

Fig. 1. Sketches of the (a) lateral and (b) top view of the experimental setup used to observe the shear band thickness during the triaxial tests using three cameras positioned at different angles around the triaxial cell.

for each test and has usually dimensions of 80 mm vertically and 60 mm horizontally. A reference distance is marked and measured on the filled membrane before the test and is used to calibrate the size of the pixels from the pictures. In the present tests, the photographic resolution is about 0.02 mm/pixel. The window used for the digital correlation is then divided into a regular mesh of squares between 25 and 40 elements in each directions (depending on the grain size). The characteristic patterns inside these squares is sought into the next picture using the Normalized Cross-Correlation defined as:

$$NCC(u,v) = \frac{\sum_{x,y} I_1(x,y) I_2(x-u, y-v)}{\sqrt{\sum_{x,y} I_1(x,y)^2 \sum_{x,y} I_2(x-u,y-v)^2}} \quad (1)$$

where I_1 and I_2 are the two successive pictures n and n+1 considered as matrices. x and y are the coordinates of the images. u and v are the integer displacement values to apply respectively to the x and y components of image I_2. The coordinates (u,v) that give the maximum of the cross-correlation function represent the best estimate of a subsets displacement. Sometimes, this cross-correlation functions leads to unrealistic displacements. These errors are tracked by comparing the value at each point with the displacements obtained at other points in a region surrounding the point. If this value is too different (four times more), the value of the displacement obtained from the cross-correlation is replaced by an interpolation from the displacements of the surrounding nodes.

In order to estimate the size of the shear band, localization is traced from the profile of the maximum shear strain and the increment of deformation field in the vertical direction $\Delta\varepsilon_{yy}$ is evaluated by calculating the ratio of the difference of displacements between two successive points on the mesh vertically and the distance between them (see Appendix B for a more detailed explanation and rationale of the calculations of the different strain increments). This field of strain increment ($\Delta\varepsilon_{yy}$) enables to obtain the same results for the shear band thickness as the maximum shear strain or the volumetric strain increments, but the data are generally cleaner that is why this field has been chosen in the following. Following this step, three cuts of this variable along the x and y axes are considered (horizontal and vertical) as shown in Figure 2b by picking points (1,2 and 3 in Figure 2b) that are located on the shear band. The least square methods is then used to interpolate the deformation field in these sections with a Gaussian equation 2, as shown in Figure 2c (Gudehus and Nubel, 2004).

$$\Delta\varepsilon_{yy}(x_i) = K_i e^{-(\frac{x_i - \mu_i}{\sigma_i})^2} \quad (2)$$

where μ_i, σ_i and K_i are the expect value, the variance and the amplitude of the gaussian distribution respectively. x_i corresponds to the coordinates along x and y depending on the direction of the cross-section. The variance σ_i corresponds to the width halfway up the Gaussian, and therefore the full width of the gaussian in one of the cut considered can be calculated by (Rattez et al., 2018c):

$$w_i = 2\sqrt{2ln(2)}\sigma_i \quad (3)$$

The values of the width of the gaussian in the horizontal and vertical directions in the three cross-sections (as shown in

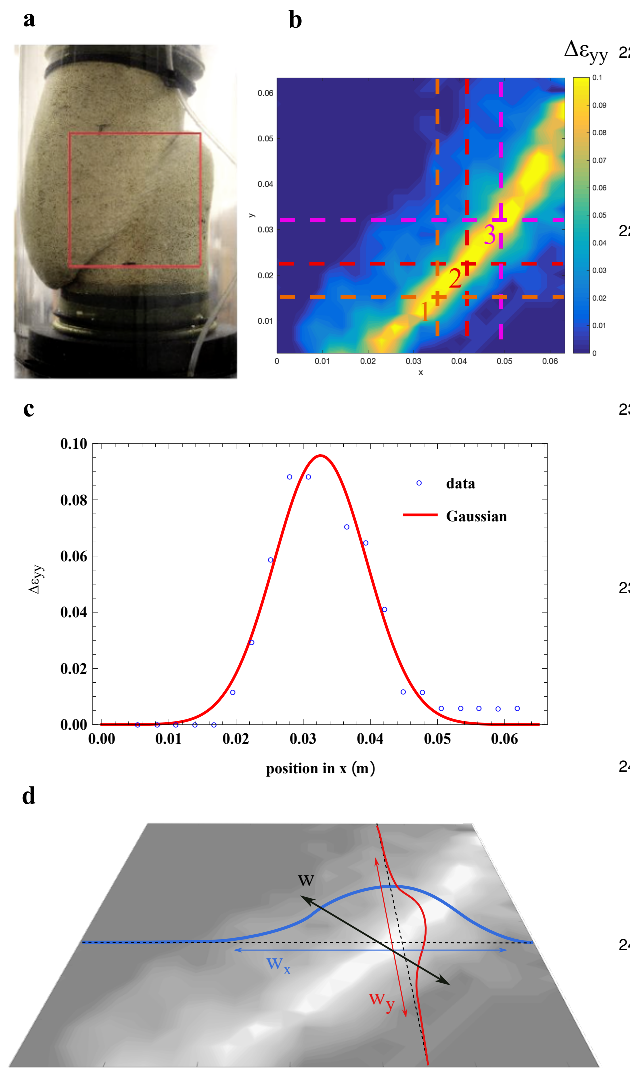

Fig. 2. Digital image correlation applied to the triaxial test to evaluate the shear band thickness evolution. a) Example of picture taken from one of the camera at the end of a test showing a shear band and the window (red), in which the DIC is applied. b) Example of deformation increment field $\Delta\varepsilon_{yy}$ obtained for the picture in a) showing the 3 points and the associated cross-sections in the x and y directions used for the shear band width assessment. c) Example of fitting by a gaussian function of the deformation data for one cross-section. d) Schematic representation for the calculation of the shear band thickness from the horizontal and vertical cross-sections and the gaussian fitting.

Figure 2d) enable to assess the actual width of the shear band w for a given cross-section from the relation:

$$w = \frac{w_x \, w_y}{\sqrt{w_x^2 + w_y^2}} \qquad (4)$$

The final value of the shear band thickness for a given time step is then calculated as the mean of the values obtained from the three points considered (Figure 2b). This value is validated against the results of two other methods to ensure correctness of the calculations, as explained in Appendix C.

Materials used

The sand used for the experiments is a standard sand used for concrete and is composed of silica round-shaped grains. The samples tested in this study are shown in Figure 3, which exhbits the cumulative percentage of finer particles as a function of the grain size in logarithmic scale. The particle size distribution of the initial sand corresponds to the sample referred as ”w3” in Figure 3 middle. This initial particle size distribution is modified by adjusting the weight of particles retrieved between two sieves following the ASTM standard (ASTM D422) to obtain the different samples. Three sets of materials have been tested in this paper. The four samples labeled ”uniform” are composed of particles obtained between two consecutive sieves (or three in the particular case of u4) and are therefore homogeneous in terms of grain diameters. They are named u1 to u4 and u1 is the samples containing the largest grains (see Figure 3 top). The five samples labeled ”graded” are obtained by modifying the initially graded by changing the fractions of small and large particles from the initial sand in order to create another graded sand with a different mean grain size. These samples present a quite symmetrical distribution of sizes for the larger and smaller particles compared to the mean grain size (in the logarithmic scale).

The last set of five different samples are called ”fractal” (Figure 3 bottom). This term refers to distributions that present a power law for the number of particles between two consecutive sieves as a function of the mean grain diameter of these grains. The number of particles for a given sieve (and thus for a given grain diameter calculated as the mean between the two subsequent sieves) is obtained by assuming the particles to have a spherical shape and the material density to be the same for all the particles (2650 kg/m^3). The ratio between the weight of sand retained by the sieve and the weight of a grain with the diameter equal to the average between the mesh aperture of sieve and the overlying sieve enables to obtain an estimation of the number of particles.

The fractal dimension (F) is defined by $N(D) = D^F$, where N is number of particles of diameter D (Sammis et al., 1987). The concept of fractal dimension is based on the notion of self-similarity. An object, or a figure, can be defined as self-similar if it looks essentially identical at all scales it is observed or, in other words, if it can be divided in a certain number of parts which are similar to the original one. In the case of granular materials, it was first observed that fault zones' samples reveal a remarkable degree of self-similarity for the grain size distribution (Sammis et al., 1987; Turcotte, 1989). The authors have found the fractal dimension to be around 1.60 in two-dimensional cross-section, corresponding to a dimension of 2.60 in three dimensions. On the basis of these observations, they have proposed a comminution model, for the mechanical processes that generate fault gouges. Self-similarity results from repeated tensile splitting of grains and the fact that the splitting probability depends largely on the relative size of nearest neighbors: during the fragmentation process, the direct

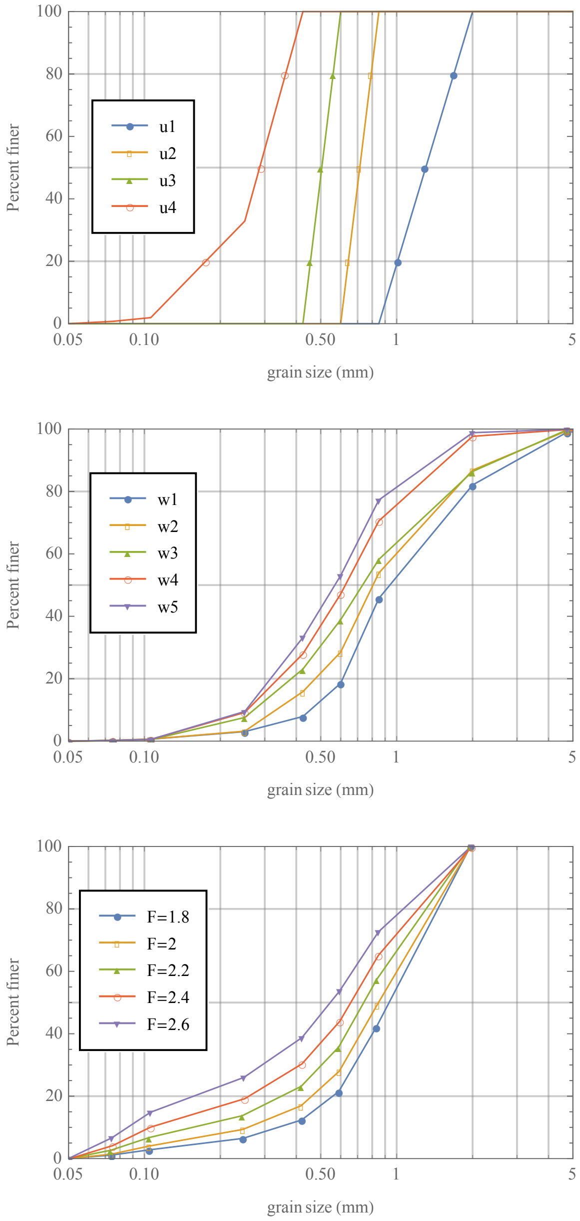

Fig. 3. Cumulative particle size distributions for the (top) uniform, (middle) graded, (bottom) fractal samples used in this study.

contact between two particles of near equal size will result in the tensile breakup of one of the two. However, a large particle surrounded by smaller particles has a a larger coordination number, which induces a cushion effect (McDowell et al., 1996) and makes them more resistive to crushing. This topological effect leads to a final state of the particle size distribution, for which the fragmentation process is inhibited (Einav, 2007). The material exhibits a particle distribution in which particles of the same size are geometrically separated from each other. Such a spatial organization repeats itself at each scale, providing a self-similar grain size distribution and a fractal dimension of 2.58, independently of the initial size distribution of the particles (Sammis et al., 1987). In the present study, the process of breakage is assumed to be negligible as a silica sand composed of strong particles is used and confined with a low confining

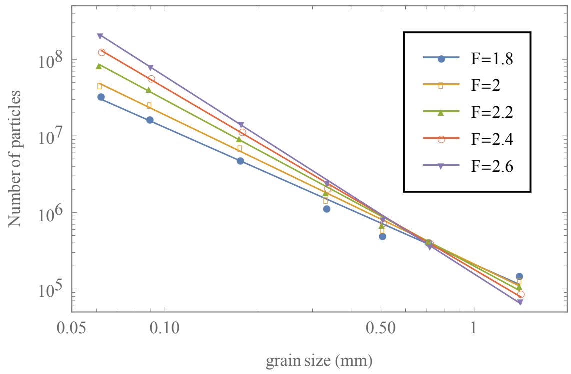

Fig. 4. Number of particles for 1 kg of sand as function of the grain diameter for the fractal samples. The points represent the experimental data obtained from sieves. The lines represent an interpolation of the experimental data using a power law with an exponent equal to the fractal number.

pressure (Karimpour and Lade, 2010) even though particle distributions that result from this mechanism are used. Thus, the aim of this study is to look at the effect of a non-evolving particle distribution on the process of strain localization and isolate this effect.

The number of particles for 1 kg of sand as a function of the grain diameter is shown in Figure 4, together with fitting by a power law. The number of particles for a given sieve (and thus for a given grain diameter calculated as the mean between the two subsequent sieves) is obtained by assuming the particles to have a spherical shape and the material density to be the same for all the particles (2650 kg/m^3). The ratio between the weight of sand retained by the sieve and the weight of a grain with the diameter equal to the average between the mesh aperture of sieve and the overlying sieve enables to obtain an estimation of the number of particles. The samples presenting a power law exponent different from 2.6 are also called fractal by extrapolation even though they are not self-similar.

RESULTS AND DISCUSSIONS

In this section, the results obtained for the triaxial tests are presented in terms of load-displacement, shear band thickness evolution and residual shear band size.

Mechanical results

In Figure 5, the load-displacement response for the different particle size distributions tested is reported. All the specimens exhibit a similar behavior before reaching the peak. For the uniform, graded and fractal distributions, the value of the peak load decreases with the size of the grains. The largest peak is observed for u4 with a mean grain size D_{50} of 0.3 mm and the smallest peak is observed for u1, w1 and the fractal number 1.8 with a D_{50} of 1.05, 0.95 and 0.96 mm respectively. The softening of the load after the peak tends to be less important with the increase of D_{50}, and almost vanishes for the samples u1, w1 and the fractal number 1.8.

Although the linear part and the peak are mostly reproducible (see Figure 7), the softening branch is sensitive to the number of shear bands developing, thereby inducing small randomness in the post-peak behavior. In general, it is observed that the presence of more than one shear bands induces a less pronounced softening branch, as explained in Bésuelle et al. (2006). It should be noted that the results shown here correspond to tests for which one dominant shear band could be identified and measured. Tests for which multiple shear banding was more pronounced were discarded. Moreover, the axial displacement applied to the sample at the peak presents an increase with the mean grain size. Finally, the broadness of the distribution does not influence the shear strength and softening behavior of the samples, at least in the range of the tested D_{50} and distributions considered. A similar influence of the grain size has been observed by Harehdasht et al. (2017) for drained triaxial experiments performed on glass beads and Péribonka sand.

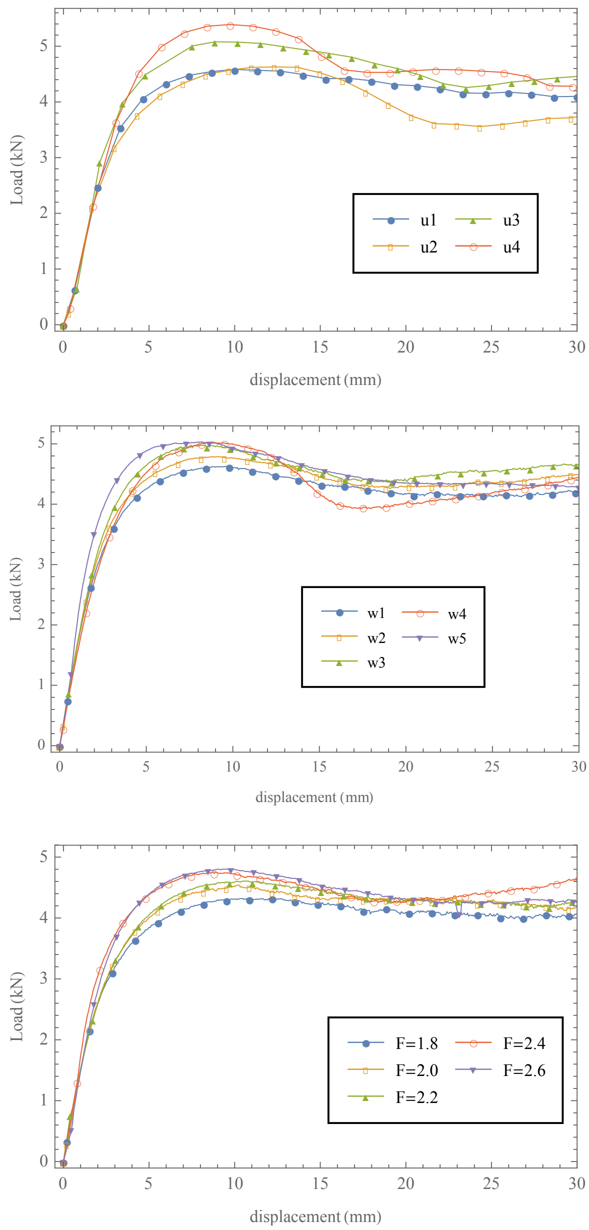

Fig. 5. Load-displacement responses obtained for (top) uniform distribution; (middle) graded; (bottom) fractal distribution samples.

Shear band evolution

The mechanical tests that have been performed in this study have enabled to obtain the stress-strain response of the samples together with the evolution of the shear band thickness. In Figure 6, an example is shown of the stress-strain response obtained for a sample presenting a uniform distribution and a mean grain size D_{50}=0.7 mm (sample u2). In Figure 6b, the fields of deformation obtained at different stages of the tests are also represented. The triggering of localization is observed when the material nears its peak value for the shear strength at stage 2. However, the fitting with the gaussian function presented in the previous section does not enable to capture this nucleation as the deformations are still distributed into the sample, which makes it difficult to distinguish this triggering from the noise in the deformation data. Precise observations with X-ray tomography scans realized at different stages of loading coupled with digital volume correlation enable to obtain a better insight into the beginning of localization (Desrues et al., 2018). Desrues et al. (2018) could observe numerous planar regions of localization concurrently active just before the peak stress, and for accurate identification of the onset of localization such approaches should be preferred. Because of their radiographic nature and accuracy, these observations take more time and are more complicated in terms of post-processing than the the methodology presented here, which can be realtively easily applied to a large number of tests, when the determination of the post-onset evolution of localization is of interest.

In the softening phase, the deformation localizes in a thinner zone. The shear band size has been captured just before stage 3 (Figure 6a), when the localization into one band becomes clear on the map of the deformation increment field $\Delta\varepsilon_{yy}$. The shear band thickness tends to a steady value at the end of the softening phase. The representations of $\Delta\varepsilon_{yy}$ at stage 5 and stage 6 show clearly that the shear band size is not evolving, it is just shifted toward the left due to the vertical motion of the piston that moves the specimen compared to the window where the DIC is applied, which is maintained at the same position.

In Figure 7, several samples presenting a uniform distribution and a mean grain size D_{50}=0.7 mm (distribution u2) have been tested to evaluate the reproducibility of the results. Both the load-displacement reponse and the shear band thickness evolution have a similar behavior between the different tests. In particular, all the samples reach a residual shear band thickness between 21 and 23 mm of axial displacement applied to the sample. Moreover, the residual shear band thickness calculated as the mean of the values once the plateau is reached lie between 6.4 and 8.1 mm, with the latter obtained for u3c, which is the only one presenting slightly

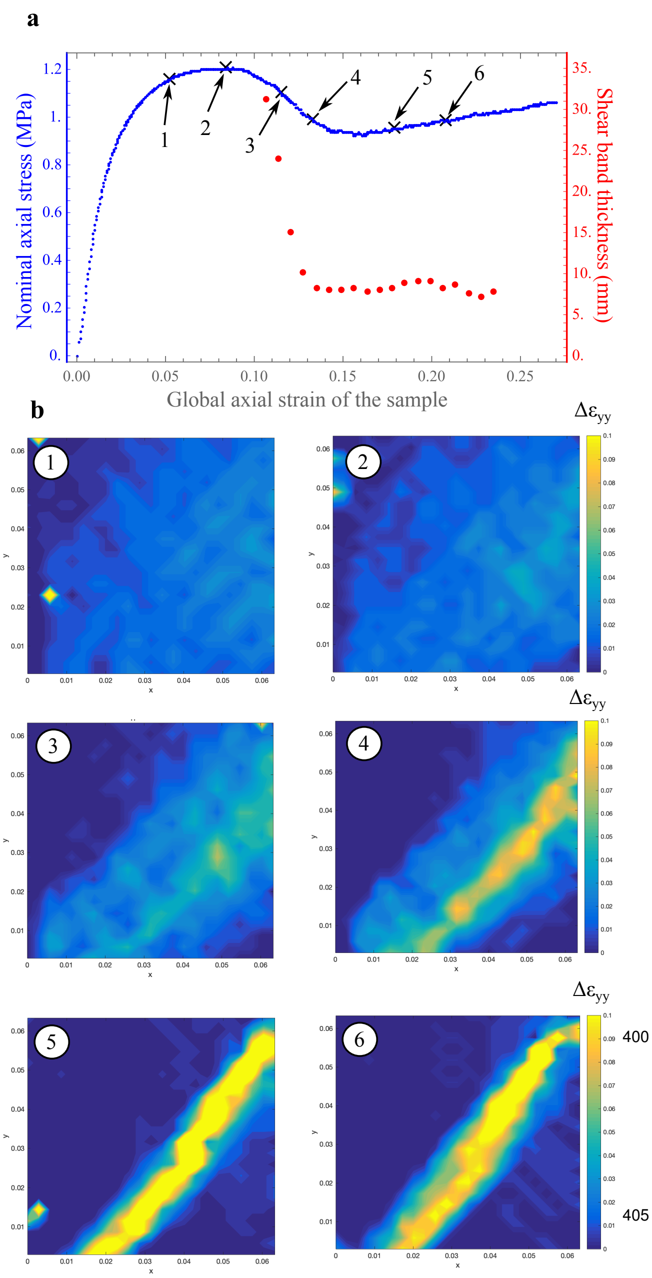

Fig. 6. Results obtained for the uniform sample u2 showing a) the stress-strain response of the sample together with shear band thickness evolution b) the field of deformation $\Delta\varepsilon_{yy}$ at different stages of loading indicated in a) showing the evolution of the shear band.

larger values compared to the other tests. Note that all the results presented in the following have been reproduced by at least two independent experiments, with minimal deviations among them and one selected case for each sample is shown.

In Figure 8, the shear band thickness evolution obtained for the different samples is plotted. All the samples showcase a decrease of the shear band thickness before attaining a steady state value. The smoother evolution curves of the shear band size are obtained for the uniform samples, as compared to the fractal and graded samples. It is observed that the larger the mean grain size is, the more displacement is required for the shear band to appear and reach a steady state. This is due to the shifting in terms of displacement of the maximum of the shear stress for the larger grains (as shown in Figure 5). In the case of u1, the decrease of the shear band thickness is happening after the softening phase, which is not very pronounced, because the sample exhibits barreling before a shear band appears. It can also be noticed that the smaller the D_{50} is, the smaller the residual shear band size gets. The graded sample w2 does not follow this trend, it displays a late decrease and presents a residual shear band width in between w4 and w5. However, the repeated tests for w2 were noisier but seem to indicate that the residual shear band size should be larger (at least larger than the one for w4). Moreover, the sample with a fractal dimension 2.0 showcases a smaller residual thickness than F=2.2, but this difference remains quite close.

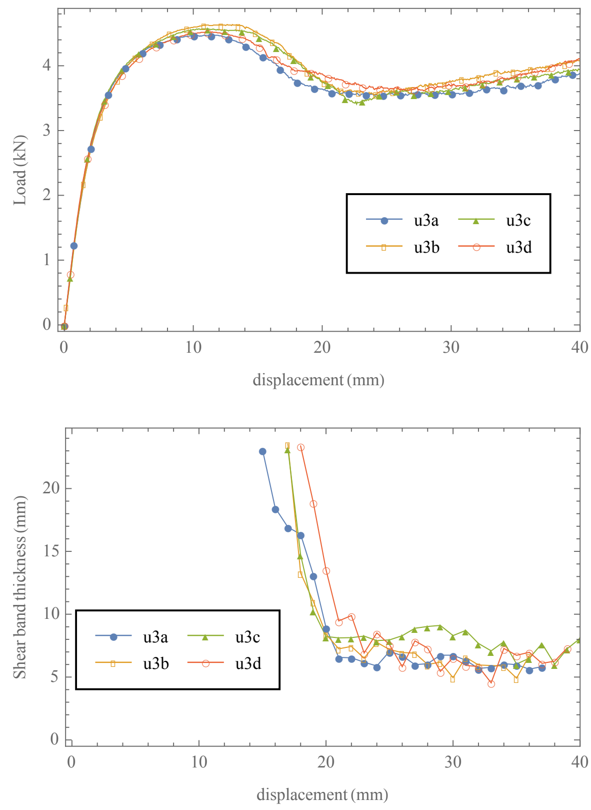

Fig. 7. Results for the load-displacement response (top) and the shear band thickness evolution (bottom) for the sample u2 repeated several times to estimate the resproducibility of the results.

Residual shear band thickness

In Figure 9, the results for the residual shear band thickness calculated as the mean of the residual thickness values are presented for the uniform, graded and fractal distributions as a function of the mean grain size. The different markers correspond to the different types of distributions and the dashed lines are the median values of the ratio of the residual size to D_{50} calculated for the uniform, graded and fractal distributions independently. The residual shear band sizes for the uniform distributions show a value very close to $10 \times D_{50}$ for all cases

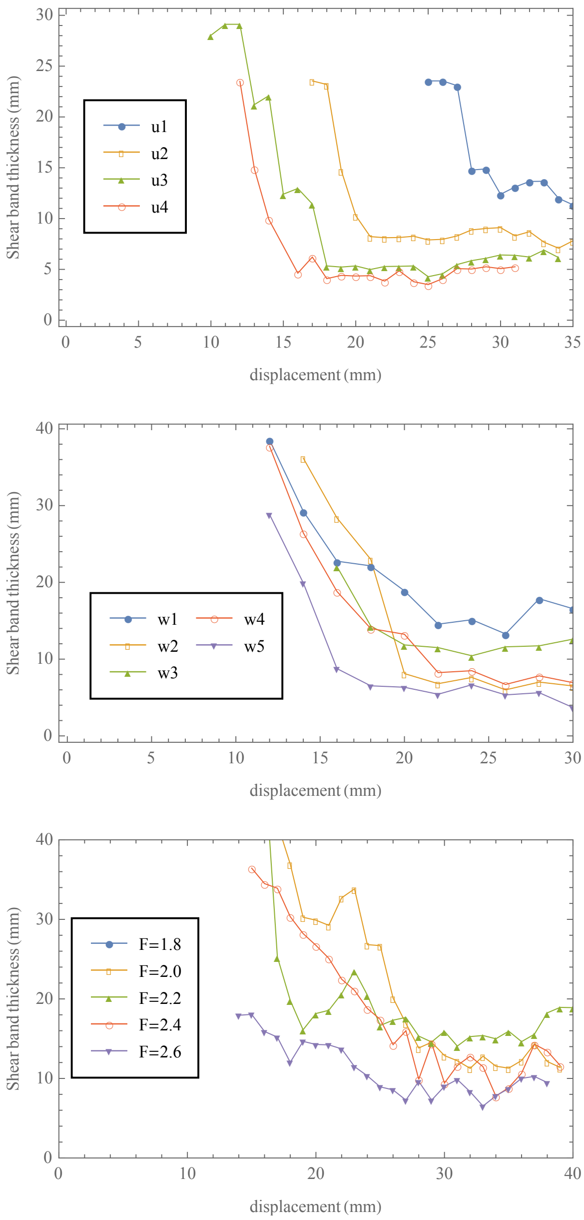

Fig. 8. Shear band thickness evolution as a function of the displacements obtained for (top) uniform distribution; (middle) graded; (bottom) fractal distribution samples.

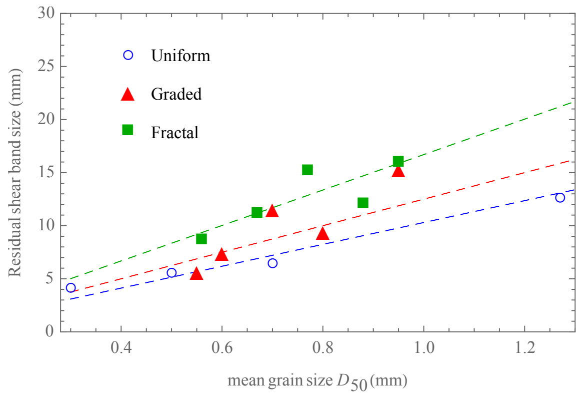

Fig. 9. Residual shear band thickness w_r obtained for the uniform, graded and fractal distributions as a function of the mean grain size (points) and the interpolation by a linear function for each distribution (dashed lines). The blue line (median of uniform distributions) corresponds to $w_r = 10.3 \times D_{50}$, the red line (median of graded distributions) to $w_r = 12.5 \times D_{50}$ and the green line (median of fractal distributions) to $w_r = 16.7 \times D_{50}$.

(the dashed line has a slope of 10.3). In comparison in the case of the graded samples, the values are scattered and the ratios of the residual shear band thickness to the D_{50} lie between $9 \times D_{50}$ (for w2) and $16 \times D_{50}$. The median value of the ratio is 12.5, which is larger than the uniform distributions. Finally, for the fractal distributions the residual shear band thickness scales satisfactorily with the D_{50} despite the fact that a different fractal dimension imply a different broadness of the distribution, and the median value for this scaling is $16.7 \times D_{50}$, significantly larger than for uniform samples.

The scaling of the residual shear band thickness with the mean grain size confirms previous studies on the subject (Roscoe, 1970; Scarpelli and Wood, 1982; Mühlhaus and Vardoulakis, 1987; Tatsuoka et al., 1990) and shows that this observation seems to hold for wider distributions like fractal distributions in the conditions of the experiments presented here.

Upon calculation of the dependence of the ratio of the shear band thickness to D_{50} on the coefficient of uniformity $Cu = D_{60}/D_{10}$, shown in Fig. 10, a linear scaling of this ratio is obtained with Cu. As Cu increases from around 1 (uniform distributions), through graded distributions ($Cu \sim 2-4$) to well graded fractal distributions ($Cu > 4$), the shear band thickness passes from $10 \times D_{50}$, all the way to $16.7 \times D_{50}$. This transition implies that broader distributions tend to admit thicker shear bands. Such a response could stem from the fact that in the case of broad distributions, like the fractal ones, the morphology of the forces network between particles is more ramified compared to a narrower distribution as shown in Mair and Hazzard (2007). In that study, Mair and Hazzard (2007) have performed three dimensional discrete element simulations on different granular size distribution (from narrow to fractal 2.6) and show that granular media with wide size distribution present more distributed tree- or sheet-like force networks that have significant out-of-plane linkage and appear to enjoy a wider spread of orientations. This effect would tend to enlarge the shear band thickness and explain the larger scaling observed here. However, in their simulations, Mair and Hazzard (2007) did not observe any strain localization, and for this reason further analyses of the force networks developing in the shear bands with dicrete element methods or X ray CT-scanner, would be required to verify this hypothesis.

Another hypothesis for explaining why broader distributions would admit thicker shear bands relies on a suggestion of Wichtmann and Triantafyllidis (2013). In that study, Wichtmann and Triantafyllidis (2013) argued that in polydisperse materials parts of the smaller grains with weak contacts will probably show a rolling contact behavior, since the small grains will act as a kind of lubricant for the larger grains. In this case,

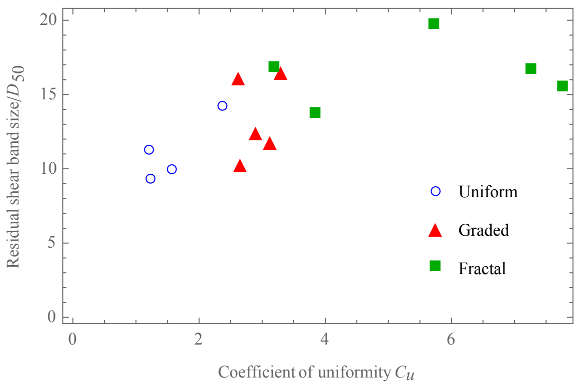

Fig. 10. Ratio of the residual shear band thickness h_r obtained for the uniform, graded and fractal distributions and the mean grain size as a function of the coefficient of uniformity C_u.

the rolling mechanism induce larger non-local interactions between the grains compared to intergranular sliding and tends to enlarge the thickness of the shear band (Papanicolopulos and Veveakis, 2011).

CONCLUSIONS

In this study, standard triaxial experiments have been conducted on dry sand to investigate the influence of the particle size and the particle distribution on the shear band thickness at low confinement.

The field of deformation obtained from the displacements of elementary cells identified on the membrane of the sample has been fitted by a gaussian distribution, which has enabled to observe the evolution of the shear band thickness. This methodology is not accurate enough to observe precisely the beginning of localization. However, it enables to capture the shear band thickness evolution once a band starts to develop sufficiently and relate it to the stress-strain response and the initial particle size ditribution. This information is important for models aiming at describing the localization in geomaterials and can allow them to compare their results with the stress-strain and the shear band thickness evolution.

The shear band thickness exhibits a rapid decrease until reaching a residual value at the end of the stress softening regime or for larger displacements depending if some barreling is triggered before the localization. It is observed that the residual shear band thickness scales with the mean grain size satisfactorily for the uniform and fractal distributions in the conditions of the experiments presented here. The ratio of the residual shear band thickness to the mean grain size D_{50} exhibits a value around 10 for uniform distributions and 17 for fractal distributions.

All these results enable to give an insight into the questions raised in the introduction: (i) The residual shear band thickness scales with the mean grain size but this scaling depends on the coefficient of uniformity of the distribution. (ii) The addition of fine grains causes an increase of the wideness of the grain size distribution and leads the shear band to achieve thicker values, presumably due to wider force chain networks and/or significant rolling induced by the smaller particles. (iii) The mean grain size and coefficient of uniformity should be considered as parameters in models aiming at capturing strain localization.

ACKNOWLEDGEMENTS

This work was supported by the Southern California Earthquake Center (SCEC), award number 118062196. SCEC is funded by NSF Cooperative Agreement EAR-1033462 and USGS Cooperative Agreement G12AC20038.

APPENDIX A: INFLUENCE OF OPTICAL EFFECTS ON THE MEASUREMENTS

The source of errors for the calculation of the strain field and the shear band thickness in terms of imaging and digital image correlation can be of four types:

- Distortion of the images due to the camera lens.
- Geometrical effects due to the cylindrical shape of the samples in the triaxial test.
- Refractions at the interfaces of the plexiglas and the water inside the confining chamber that induce a magnifying effect on the images.
- Error in the cross correlation analysis for a subset between two subsequent images.

In the following, these four sources of errors for the calculations of the deformation fields and shear band thickness are discussed and their effects are quantified.

The optical parameters of the cameras used for the image analysis have been calibrated using the Camera Calibration Toolbox for MATLAB (Bouguet, 2008). Pictures of a planar checkerboard with known dimensions are taken with the cameras at different positions and orientations, keeping the camera stationary. The set of pictures enables to calculate the parameters of the cameras and then correct the images. In the present case, the difference between the inital and corrected images is very small (modification of a few pixels on the side of the picture), therefore the distortion is negligible.

To take into account the cylindrical shape of the samples and the refraction in the displacements and distances calculations, the approach of (Bhandari et al., 2012) is followed. First, a ray tracing method is applied to determine the locations of equidistant points on a planar image tangent to the outer cell wall and perpendicular to the optical axis of the camera are located on the surface of the specimen. The rays originate from the pinhole of the camera, pass through the points on the planar image, are refracted at the interface air-plexiglas and plexiglas-water before reaching the surface of the specimen (see Figure 11). As the rays close to the optical axis of the camera are not refracted and reach the specimen almost perpendicularly, the distances in this region of the image are similar to the

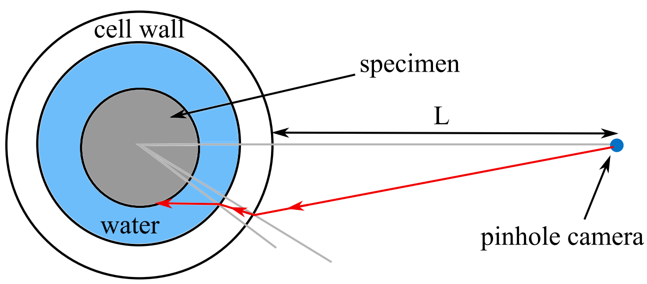

Fig. 11. Schematic representation of the ray-tracing and refraction for the experiments.

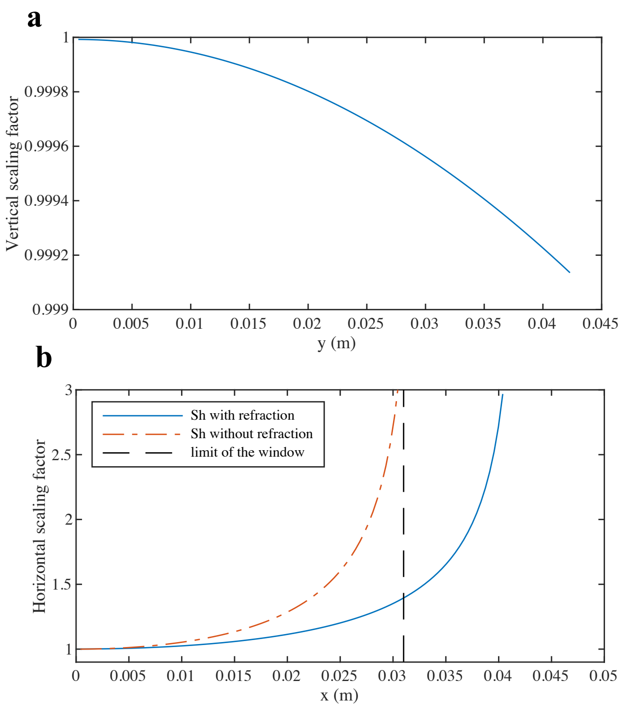

Fig. 12. Scaling factors for the displacements and distances calculated on the images of the cameras in the: a. vertical direction b. horizontal direction (with and without refraction).

distances on the specimen. However, further from the optical axis, the curvature of the specimen and the refraction induce variations in the distances between adjacent points of the planar image compared to the real distance on the surface of the specimen. Thus, scaling factors (horizontal S_h and vertical S_v) must be applied to components of displacement vectors and the coordinates at the measurement points determined using the digital image correlation technique as explained in (Bhandari et al., 2012). The scaling factors are defined by the ratio of the spacing of measurement points on the specimen surface by the spacing of measurement points on the image plane and it is refered to Bhandari et al. (2012) for more details on their calculations.

In Figures 12a and 12b, the evolution of the vertical and horizontal scaling factors with the distance on the planar image respectively is shown. The scaling factors are calculated for only one fourth of the image as the rest can be determined by symmetry, using a spacing of 0.5 mm between the points on the planar image. The zero in the x and y axes in Figure 12 correspond therefore to the center of the planar image and the position of the optical axis of the camera. It can be observed that the vertical scaling factor is negligible as the ratio of vertical distances of the planar images compared to the the distances on the specimen differ of 0.1 % at maximum. For the horizontal scaling factor, the refraction tends to decrease the effect of the cylindrical shape of the samples by reducing the scaling factor. in Figure 12 b, the limit of the window used to perform the cross correlation analysis between subsequent images is represented and a scaling factor of almost 1.4 is obtained at the edge of this window.

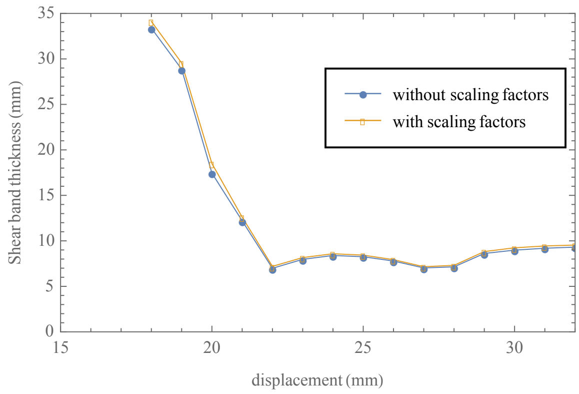

Fig. 13. Comparison for the evolution of the shear band thickness with displacement for the specimen u2 considering or not the horizontal scaling factor for the distances and displacements.

The horizontal scaling factor has been used to correct the values of the displacements obtained from the digital image correlation and the distances between the points in the horizontal direction for the sample u2. In Figure 13, it is shown the comparison between the evolution of the shear band thickness calculated with and without considering the scaling factor as a function of the vertical displacement. Despite the non negligible value of the horizontal scaling factor on the edges of the window of correlation, the fact that cross-sections are used here in which the shear band is located closer to the center of the image than to the edge (the optical center is located at 0.03m on the x-axis of the map of the deformation field) leads to a negligible effect of this factor on the shear band thickness calculations. The error due to the refraction and the cylindral shape is around 3 % for the shear band thickness and is thus neglected in this paper.

It is to be noted that the experiments have been performed with membranes of 2 different thicknesses (0.012 and 0.025) and the results were identical. Therefore, it can be concluded that the distortion of the membrane is not significantly affecting the results.

Finally, the increment of displacements between two images is calulated using maximum of the correlation function defined in Equation 1, but the noise on the images can lead to local maxima and displacements that are unrealistic. This effect appears mostly on the edge of the window where the image resolution presents a lower quality. In order to remove some of these errors in the map of increment of displacement field, they are located by comparing local displacements to the average norm of the displacements. If a single vector of displacement has a norm much larger than the average value and larger than its neighbors, it is replaced by an average value of displacements from the neighboring points (without including other points presenting an error).

APPENDIX B: INFLUENCE OF THE DIFFERENT STRAIN FIELDS ON THE SHEAR BAND THICKNESS CALCULATION

In this Appendix, the method to calculate the vertical, volumetric and shear strain fields presented and all of them are used to calculate the shear band thickness and their results compared.

From the vector of increment of displacement obtained for each points of the discretized image, the increment of strain tensor in two dimensions can be calculated following the small strain theory:

$$\overline{\overline{\Delta\varepsilon}}(x,y) = \begin{bmatrix} \frac{\partial u}{\partial x} & \frac{1}{2}(\frac{\partial u}{\partial y} + \frac{\partial v}{\partial x}) \\ \frac{1}{2}(\frac{\partial u}{\partial y} + \frac{\partial v}{\partial x}) & \frac{\partial v}{\partial y} \end{bmatrix} \tag{5}$$

where u and v are the horizontal and vertical components of the increment of displacement vector respectively. The partial derivatives are approximated by a forward difference. The principal strain increments are therefore (Bhandari et al., 2012):

$$\Delta\varepsilon_1 = \frac{1}{2}(\Delta\varepsilon_{xx} + \Delta\varepsilon_{yy} + \sqrt{(\Delta\varepsilon_{xx} - \Delta\varepsilon_{yy})^2 + \Delta\varepsilon_{xy}^2}) \tag{6}$$

$$\Delta\varepsilon_3 = \frac{1}{2}(\Delta\varepsilon_{xx} + \Delta\varepsilon_{yy} - \sqrt{(\Delta\varepsilon_{xx} - \Delta\varepsilon_{yy})^2 + \Delta\varepsilon_{xy}^2}) \tag{7}$$

which enables to calculate the maximum shear strain increment and the volumetric strain increment (assuming that the radial strain increment is equal to the hoop strain increment):

$$\Delta\gamma_{max} = \Delta\varepsilon_1 - \Delta\varepsilon_3 \tag{8}$$

$$\Delta\varepsilon_v = \Delta\varepsilon_1 + 2\Delta\varepsilon_3 \tag{9}$$

In Figure 14, maps are shown of the displacement increment, the axial strain increment $\Delta\varepsilon_{yy}$, the maximum shear strain increment and the volumetric strain increment for the uniform sample u2 at four different time steps (refered in Figure 6) to illustrate how the process of localization can be captured by the different fields. For this sample, the shear band thickness is assessed using the three cross-sections and the fitting with a gaussian distribution. An example of distribution for a given time step and a given cross section along the vertical axis is shown in Figure 15. For the three fields of deformation, the distributions exhibit a similar width, but different amplitudes. The evolution of the shear band thicknesses can be assessed from the axial, volumetric and maximum shear strain increments during the test. In Figure 16, it is shown that the evolution of the shear band size does not depend on the field of deformation chosen to calculate it.

APPENDIX C: SHEAR BAND THICKNESS EVALUATION WITH A THRESHOLD

Another method has been used to evaluate the shear band thickness. This method relies on defining a threshold value and is therefore more in the paradigm of the shear band seen as a thin layer that is bounded by two parallel material discontinuity surfaces of the incremental displacement gradient as described in Hill (1962). The material discontinuity surfaces are the shear-band boundaries and their distance can be defined as the shear band thickness (Vardoulakis and Sulem, 1995).

By defining a threshold value (here chosen as one fifth of the maximum strain), the increment of deformation map can be converted into a binary image, in which the points above this value are given the value 1 and the points below the value 0. After this segmentation of the strain field for each time step, the morphological algorithm is used to find the minimum rectangle surrounding the zone containing only values 1. An example of the box obtained on top of the map of increment of axial strain is shown in Figure 17. From the distance between the two edges of the rectangle, the shear band thickness can be calculated. The results obtained from this method called the ”box method” in terms of evolution of the shear band thickness for sample u2 is shown in Figure 18. This method enables to obtain a shear band thickness evolution with displacements in agreement with the fitting of a gaussian distribution used in this paper. However, it is more difficult to capture the onset of localization, when the shear band is not completely formed with this method as at this stage the deformations in the specimen are still quite spread. Moreover, the Box method depends strongly on the threshold value chosen and, therefore of the user, which makes it difficult to use and makes the results reproducible. It is also more subject to local error in the deformation as small variations of the values of the deformation close to the interface can make the values at those points to be or not inside the interface between the two regions and modify significantly the shear band thickness calculated.

The same residual shear band thicknesses obtained from these methods (the gaussian fitting and the box method) have been compared to visual estimations of the shear band size at the end of the tests and confirm the results obtained from the calculations by digital image correlation on the deformation of the membrane.

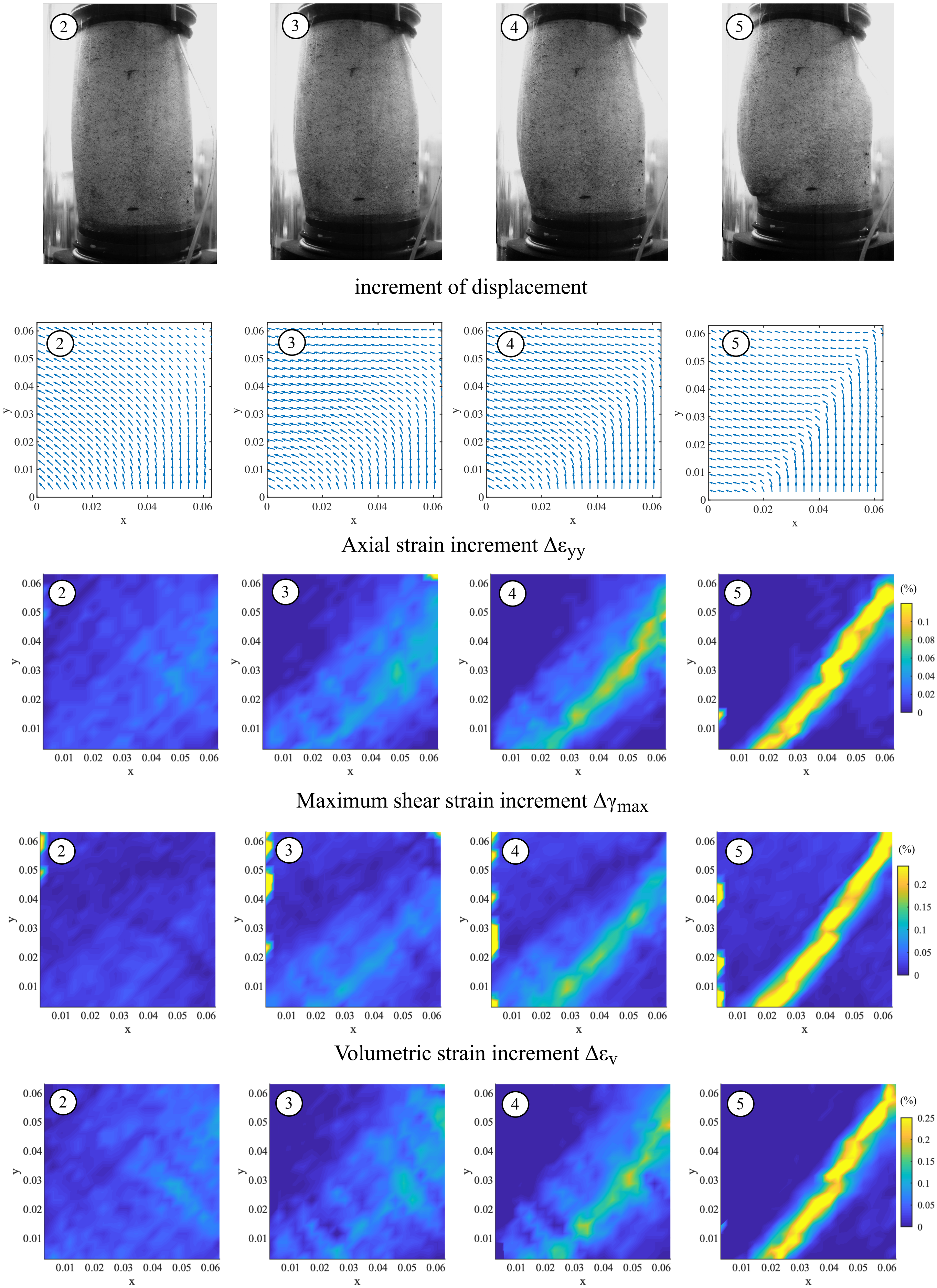

Fig. 14. Comparison of displacement and deformation fields of sample u2 at different time step.

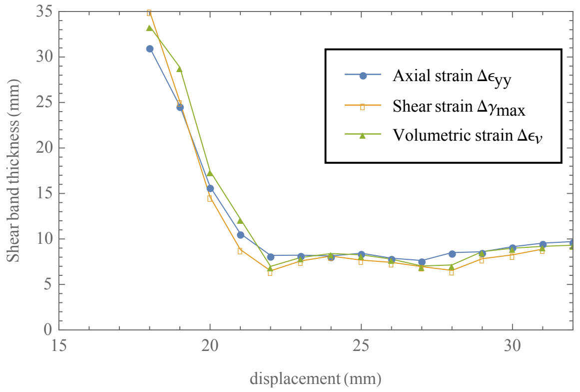

Fig. 15. Comparison of the evolution of the shear band thickness with displacement of sample u2 obtained from the different field field of strain: axial strain $\Delta\varepsilon_{yy}$, maximum shear strain $\Delta\gamma_{max}$ and volumetric strain $\Delta\varepsilon_{v}$.

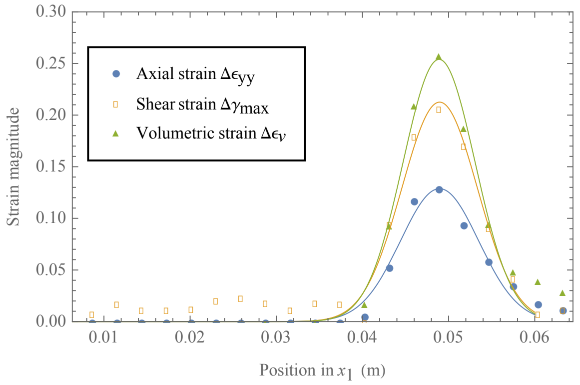

Fig. 16. Comparison of the evolution of the shear band thickness with displacement of sample u2 obtained from the different field field of strain: axial strain $\Delta\varepsilon_{yy}$, maximum shear strain $\Delta\gamma_{max}$ and volumetric strain $\Delta\varepsilon_{v}$.

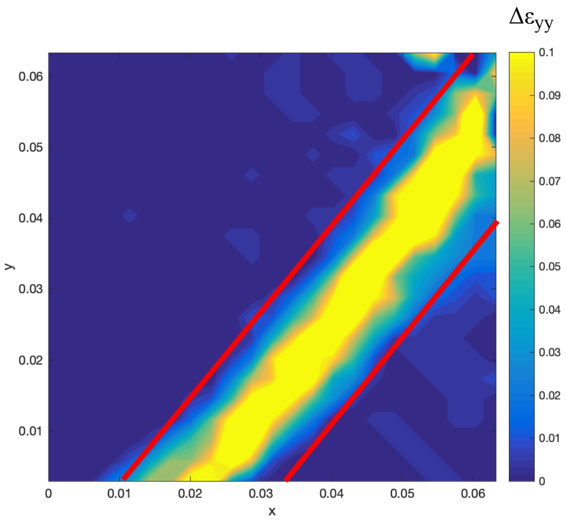

Fig. 17. Comparison of the evolution of the shear band thickness with displacement of sample u2 obtained from the fitting of a Gaussian function or a threshold value (Box method)

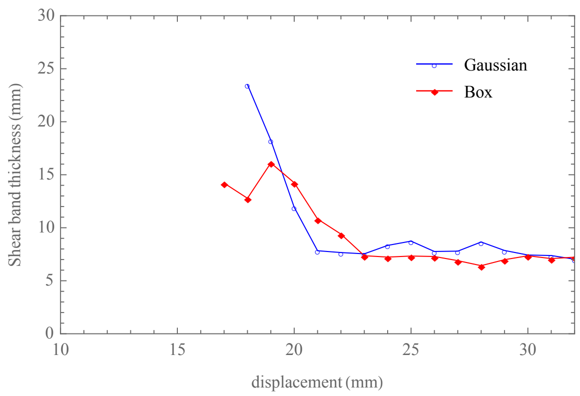

Fig. 18. Comparison of the evolution of the shear band thickness with displacement of sample u2 obtained from the fitting of a Gaussian function or a threshold value (Box method)

REFERENCES

Andò, E. (2013). *Experimental investigation of microstructural changes in deforming granular media using x-ray tomography*. PhD thesis.

Bésuelle, P., Chambon, R., and Collin, F. (2006). Switching deformation modes in post-localization solutions with a quasibrittle material. *Journal of Mechanics of Materials and Structures*, 1(7):1115–1134.

Bhandari, A. R., Powrie, W., and Harkness, R. M. (2012). A digital image-based deformation measurement system for triaxial tests. *Geotechnical Testing Journal*, 35(2):209–226.

Borja, R. I. and Lai, T. Y. (2002). Propagation of localization instability under active and passive loading. *Journal of Geotechnical and Geoenvironmental Engineering*, 128(1):64–75.

Bouguet, J.-Y. (2008). Camera Calibration Toolbox for MATLAB.

Coop, M. R., Sorensen, K. K., Freitas, T. B., and Georgoutsos, G. (2004). Particle breakage during shearing of a carbonate sand. *Geotechnique*, 54(3):157–163.

Desrues, J., Andò, E., Mevoli Ando, F. A., Debove, L., and Viggiani, G. (2018). How does strain localise in standard triaxial tests on sand: Revisiting the mechanism 20 years on. *Mechanics Research Communications*, 92(August):142–146.

Desrues, J., Chambon, R., Mokni, M., and Mazerolle, F. (1996). Void ratio evolution inside shear bands in triaxial sand specimens studied by computed tomography. *Geotechnique*, 46(3):529–546.

Desrues, J. and Viggiani, G. (2004). Strain localization in sand: An overview of the experimental results obtained in Grenoble using stereophotogrammetry. *International Journal for Numerical and Analytical Methods in Geomechanics*, 28(4):279–321.

Ehlers, W. and Scholz, B. (2007). An inverse algorithm for the identification and the sensitivity analysis of the parameters governing micropolar elasto-plastic granular material. *Archive of Applied Mechanics*, 77(12):911–931.

Einav, I. (2007). Breakage mechanics—Part I: Theory. *Journal of the Mechanics and Physics of Solids*, 55(6):1274–1297.

Gudehus, G. and Nubel, K. (2004). Evolution of shear bands in sand. *Geotechnique*, 54(3):187–201.

Guo, N. and Zhao, J. (2014). A coupled fem/dem approach for hierarchical multiscale modelling of granular media. *International Journal for Numerical Methods in Engineering*, 99(11):789–818.

Guo, N. and Zhao, J. (2016). 3d multiscale modeling of strain localization in granular media. *Computers and Geotechnics*, 80:360 – 372.

Hall, S. A., Bornert, M., Desrues, J., Lenoir, N., Pannier, Y., Viggiani, G., and Bésuelle, P. (2010). Discrete and continuum analysis of localised deformation in sand using X-ray μCT and volumetric digital image correlation. *Géotechnique*, 60(5):315–322.

Haralick, R. M. and Shapiro, L. G. (1992). *Computer and Robot Vision*. Addison-Wesley, volume ii edition.

Harehdasht, S. A., Karray, M., Hussien, M. N., and Chekired, M. (2017). Influence of particle size and gradation on the stress-dilatancy behavior of granular materials during drained triaxial compression. *International Journal of Geomechanics*, 17(9):1–20.

Hill, R. (1962). Acceleration waves in solids. *Journal of the Mechanics and Physics of Solids*, 10(1):1–16.

Karimpour, H. and Lade, P. V. (2010). Time effects relate to crushing in sand. *Journal of Geotechnical and Geoenvironmental Engineering*, 136(9):1209–1219.

Lewis, J. (1995). Fast Template Matching. In *Vision Interface*, pages 120–123.

Mair, K. and Hazzard, J. F. (2007). Nature of stress accommodation in sheared granular material: Insights from 3D numerical modeling. *Earth and Planetary Science Letters*, 259(3-4):469–485.

McDowell, G., Bolton, M. D., and Robertson, D. (1996). The Fractal Crushing of Granular Materials. *Journal of the Mechanics and Physics of Solids*, 44(12):2079–2102.

Mühlhaus, H.-B. and Vardoulakis, I. (1987). The thickness of shear bands in granular materials. *Géotechnique*, 37(3):271–283.

Papanicolopulos, S.-A. and Veveakis, M. (2011). Sliding and rolling dissipation in Cosserat plasticity. *Granular Matter*, 13(3):197–204.

Pardoen, B. and Collin, F. (2017). Modelling the influence of strain localisation and viscosity on the behaviour of underground drifts drilled in claystone. *Computers and Geotechnics*, 85(May 2017):351–367.

Rathbun, A. P. and Marone, C. (2010). Effect of strain localization on frictional behavior of sheared granular materials. *Journal of Geophysical Research*, 115(B1):B01204.

Rattez, H., Disidoro, F., Sulem, J., and Veveakis, M. (2019). Influence of dissolution on the long-term frictional properties of carbonate faults. *Preprint EarthArXiv*.

Rattez, H., Stefanou, I., and Sulem, J. (2018a). The importance of Thermo-Hydro-Mechanical couplings and microstructure to strain localization in 3D continua with application to seismic faults. Part I: Theory and linear stability analysis. *Journal of the Mechanics and Physics of Solids*, 115:54–76.

Rattez, H., Stefanou, I., Sulem, J., Veveakis, M., and Poulet, T. (2018b). Numerical Analysis of Strain Localization in Rocks with Thermo-hydro-mechanical Couplings Using Cosserat Continuum. *Rock Mechanics and Rock Engineering*, 51(10):3295–3311.

Rattez, H., Stefanou, I., Sulem, J., Veveakis, M., and Poulet, T. (2018c). The importance of Thermo-Hydro-Mechanical couplings and microstructure to strain localization in 3D continua with application to seismic faults . Part II : Numerical implementation and post-bifurcation analysis. *Journal of the Mechanics and Physics of Solids*, 115:1–29.

Rattez, H. and Veveakis, M. (2020). Weak phases production and heat generation control fault friction during seismic slip. *Nature Communications*, 11(350).

Rechenmacher, A. L. and Finno, R. J. (2004). Digital Image Correlation to Evaluate Shear Banding in Dilative Sands. *Geotechnical Testing Journal*, 27(1):13–22.

Roscoe, K. H. (1970). The influence of strains in soil mechanics. *Geotechnique*, 20(2):129–170.

Rudnicki, J. W. and Rice, J. R. (1975). Conditions for the localization of deformation in pressure-sensitive dilatant materials. *Journal of the Mechanics and Physics of Solids*, 23(6):371–394.

Sammis, C. G., King, G., and Biegel, R. L. (1987). The kinematics of gouge deformation. *Pure and Applied Geophysics*, 125(5):777–812.

Scarpelli, G. and Wood, D. M. (1982). Experimental observations of shear band patterns in direct shear tests. In *Deformation and failure of granular materials. IUTAM symposium, Delft.*, number January 1982, pages 473–484.

Segui, C., Rattez, H., and Veveakis, M. (2019). On the stability of deep-seated landslides. The cases of Vaiont (Italy) and Shuping (Three Gorges Dam, China). *EarthArXiv preprint*.

Sibson, R. H. (2003). Thickness of the seismic slip zone. *Bulletin of the Seismological Society of America*, 93(3):1169–1178.

Siddiquee, M. S. A., Tanaka, T., Tatsuoka, F., Tani, K., and Morimoto, T. (1999). Numerical simulation of bearing capacity characteristics of strip footing on sand. *Soils and foundations*, 39(4):93–109.

Smith, S. A. F., Nielsen, S., and Di Toro, G. (2015). Strain localization and the onset of dynamic weakening in calcite fault gouge. *Earth and Planetary Science Letters*, 413:25–36.

Sulem, J., Stefanou, I., and Veveakis, M. (2011). Stability analysis of undrained adiabatic shearing of a rock layer with Cosserat microstructure. *Granular Matter*, 13(3):261–268.

Takano, D., Lenoir, N., Otani, J., and Hall, S. A. (2015). Localised deformation in a wide-grained sand under triaxial compression revealed by X-ray tomography and digital image correlation. *Soils and Foundations*, 55(4):906–915.

Tatsuoka, F., Ishihara, M., Di Benedetto, H., and Kuwano, R. (2002). Time-dependent shear deformation characteristics of geomaterials and their simulation. *Soils and foundations*, 42(2):103–129.

Tatsuoka, F., Nakamura, S., Huang, C.-C., and Tani, K. (1990). Srength anisotropy and shear band direction in plane strain tests of sand. *Soils and Foundations*, 30(1):35–54.

Turcotte, D. L. (1989). Fractals in geology and geophysics. *Pure and Applied Geophysics PAGEOPH*, 131(1-2):171–196.

Vardoulakis, I. (1985). Stability and bifurcation of undrained, plane rectilinear deformations on water-saturated granular soils. *International Journal for Numerical and Analytical Methods in Geomechanics*, 9(5):399–414.

Vardoulakis, I. and Sulem, J. (1995). *Bifurcation Analysis in Geomechanics*. Blackie, Glascow.

Veveakis, M., Stefanou, I., and Sulem, J. (2013). Failure in shear bands for granular materials: thermo-hydro-chemo-mechanical effects. *Géotechnique Letters*, 3(April-June):31–36.

Veveakis, M., Sulem, J., and Stefanou, I. (2012). Modeling of fault gouges with Cosserat Continuum Mechanics: Influence of thermal pressurization and chemical decomposition as coseismic weakening mechanisms. *Journal of Structural Geology*, 38:254–264.

Viggiani, G., Küntz, M., and Desrues, J. (2001). An Experimental Investigation of the Relationships between Grain Size Distribution and Shear Banding in Sand. In Vermeer, P., Herrmann, H., Luding, S., W., E., Diebels, S., and Ramm, E., editors, *Continuous and Discontinuous Modelling of Cohesive-Frictional Materials. Lecture Notes in Physics*, volume 568, pages 111–127. Springer, Berlin, Heidelberg.

Wichtmann, T. and Triantafyllidis, T. (2013). Effect of uniformity coefficient on g/gmax and damping ratio of uniform to well-graded quartz sands. *Journal of Geotechnical and Geoenvironmental Engineering*, 139(1):59–72.

Zhao, J. and Guo, N. (2015). The interplay between anisotropy and strain localisation in granular soils: a multiscale insight. *Géotechnique*, 65(8):642–656.